

LETTER TO THE EDITOR

Characterizing interstellar filaments with *Herschel*[★] in IC5146

D. Arzoumanian¹, Ph. André¹, P. Didelon¹, V. Könyves¹, N. Schneider¹, A. Men'shchikov¹, T. Sousbie², A. Zavagno³, S. Bontemps⁴, J. Di Francesco⁵, M. Griffin⁶, M. Hennemann¹, T. Hill¹, J. Kirk⁶, P. Martin⁷, V. Minier¹, S. Molinari⁸, F. Motte¹, N. Peretto¹, S. Pezzuto⁸, L. Spinoglio⁸, D. Ward-Thompson⁶, G. White^{9,11}, and C.D. Wilson¹⁰

(Affiliations can be found after the references)

Accepted: 17/02/2011

ABSTRACT

We provide a first look at the results of the *Herschel* Gould Belt survey toward the IC5146 molecular cloud and present a preliminary analysis of the filamentary structure in this region. The column density map, derived from our 70-500 μm *Herschel* data, reveals a complex network of filaments, and confirms that these filaments are the main birth sites of prestellar cores. We analyze the column density profiles of 27 filaments and show that the underlying radial density profiles fall off as $r^{-1.5}$ to $r^{-2.5}$ at large radii. Our main result is that the filaments seem to be characterized by a narrow distribution of widths having a median value of 0.10 ± 0.03 pc, which is in stark contrast to a much broader distribution of central Jeans lengths. This characteristic width of ~ 0.1 pc corresponds to within a factor of ~ 2 to the sonic scale below which interstellar turbulence becomes subsonic in diffuse gas, supporting the argument that the filaments may form as a result of the dissipation of large-scale turbulence.

Key words. ISM: individual objects (IC5146) – Stars: formation – ISM: clouds – ISM: Filaments – ISM: structure – submillimeter

1. Introduction

Understanding how stars form out of the diffuse interstellar medium (ISM) on both global and local scales is a fundamental open problem in contemporary astrophysics (see McKee & Ostriker 2007, for a recent review). Much observational progress is being made on this front thanks to the *Herschel* Space Observatory (Pilbratt et al. 2010). In particular, the first results from the Gould Belt and Hi-GAL imaging surveys with *Herschel* have revealed a profusion of parsec-scale filaments in Galactic molecular clouds and suggested an intimate connection between the filamentary structure of the ISM and the formation process of dense cloud cores (André et al. 2010; Molinari et al. 2010). Remarkably, filaments are omnipresent even in unbound, non-star-forming complexes such as the Polaris translucent cloud (Men'shchikov et al. 2010; Miville-Deschênes et al. 2010; Ward-Thompson et al. 2010). Furthermore, in active star-forming regions such as the Aquila Rift cloud, most of the prestellar cores identified with *Herschel* are located within gravitationally unstable filaments for which the mass per unit length exceeds the critical value (Ostriker 1964), $M_{\text{line,crit}} = 2c_s^2/G \sim 15 M_\odot/\text{pc}$, where $c_s \sim 0.2$ km/s is the isothermal sound speed for $T \sim 10$ K. The early findings from *Herschel* led André et al. (2010) to favour a scenario according to which core formation occurs in two main steps. First, large-scale magnetohydrodynamic (MHD) turbulence generates a whole network of filaments in the ISM (cf. Padoan et al. 2001; Balsara et al. 2001); second, the densest filaments fragment into prestellar cores by gravitational instability (cf. Inutsuka & Miyama 1997).

To refine this observationally-driven scenario of core formation and gain insight into the origin of the filamentary structure, an important step is to characterize the detailed physical

properties of the filaments seen in the *Herschel* images. Here, we present new results from the Gould Belt survey obtained toward the IC5146 molecular cloud and analyze the radial density profiles of the numerous filaments identified in this cloud. Based on a comparison with a similar analysis for the Aquila and Polaris regions, we show that the filaments of IC5146, Aquila, and Polaris are all characterized by a typical width of ~ 0.1 pc and discuss possible physical implications of this finding.

IC5146 is a star-forming cloud in Cygnus located at a distance of ~ 460 pc (Lada et al. 1999, but see Appendix A), which consists of the Cocoon Nebula, an H II region illuminated by the B0 V star BD + 46°3474, and two parallel filamentary streamers extending to the west (Lada et al. 1994). In addition to these two streamers, the *Herschel* images reveal a whole network of filaments, which are the focus of the present letter.

2. Observations and data reduction

Our observations of IC5146 were made on 29 May 2010 in the parallel scan-map mode of *Herschel*. An area of ~ 1.6 deg² was covered by both PACS (Poglitsch et al. 2010) at 70 μm , 160 μm and SPIRE (Griffin et al. 2010) at 250 μm , 350 μm , 500 μm , with a scanning speed of 60'' s⁻¹. The PACS data were reduced with HIPE version 3.0.1528. Standard steps of the default pipeline were applied, starting from the raw data, taking special care of the deglitching and high-pass filtering steps. The final maps were created using the photProject task. The SPIRE observations were reduced using HIPE version 3.0.1484. The pipeline scripts were modified to include data taken during the turnaround of the telescope. A median baseline was applied and the 'naive' map-making method was used.

Thanks to their unprecedented spatial dynamic range in the submillimeter regime, the *Herschel* images (see, e.g., online Fig. 5 and Fig. 6) provide a wealth of detailed quantitative in-

[★] *Herschel* is an ESA space observatory with science instruments provided by European-led Principal Investigator consortia and with important participation from NASA.

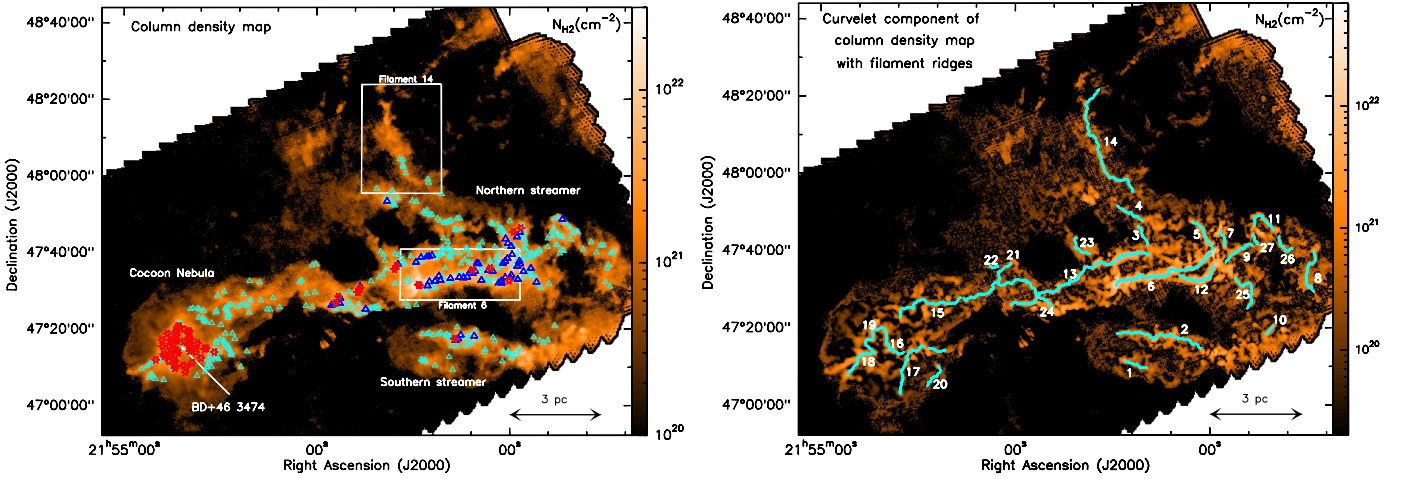


Fig. 1. (a) Column density map derived from our SPIRE/PACS observations of IC5146. The resolution corresponds to the $36.9''$ HPBW resolution of SPIRE at $500\ \mu\text{m}$. The positions of the YSOs and starless cores detected with *Herschel* (using *get-sources*, a source-finding algorithm described in Men'shchikov et al. 2010) are plotted as red stars and blue triangles respectively; bound starless cores are in dark blue (cf. Fig. 6b and Könyves et al. 2010, for classification details). The locations of the two filaments (6 and 14) whose radial profiles are shown in Fig. 2 and online Fig. 4 are marked by the white rectangles. (b) *Curvelet* component of the column density map, with the network of 27 identified filaments shown in blue.

formation on the large-scale, filamentary structure of the cloud. It is this filamentary structure that we discuss in the following.

3. Analysis of the filamentary structure

3.1. Identification of a network of filaments

Based on the *Herschel* images at five wavelengths, a dust temperature (T_d) map (see online Fig. 6a) and a column density (N_{H_2}) map (Fig. 1a) were constructed for IC5146, assuming the dust opacity law of Hildebrand (1983, see Appendix A) and following the same procedure as Könyves et al. (2010) for Aquila. We decomposed the column density map on curvelets and wavelets (e.g. Starck et al. 2003). The curvelet component image (Fig. 1b) provides a high-contrast view of the filaments (after subtraction of dense cores, which are contained in the wavelet component). We then applied the DisPerSE algorithm (Sousbie 2011) to the curvelet image to take a census of the filaments and trace their ridges. DisPerSE is a general method to identify structures such as filaments and voids in astrophysical data sets (e.g. gridded maps). The method, based on principles of computational topology, traces filaments by connecting saddle points to maxima with integral lines. From the filaments identified with DisPerSE above a 'persistence' threshold of $5 \times 10^{20}\text{cm}^{-2}$ in column density ($\sim 5\sigma$ in the curvelet map), we built a mask on the same grid as the input map, with values of 1 along the filament ridges and 0 elsewhere (cf. Sousbie 2011, for a definition of 'persistence'). Based on the skeleton mask obtained for IC5146, we identified and numbered a total of 27 filaments (shown in blue in Fig. 1b).

3.2. Radial density profiles of the filaments

To construct the mean radial density profile of each filament, the tangential direction to the filament's ridge was first computed at each pixel position along the filament. Using the *original* column density map (cf. Fig. 1a), we then measured a radial column density profile perpendicular to the ridge at each position. Finally, we derived the mean radial profile by averaging all of the profiles along the filament (see Fig. 2). In order to characterize each observed (column) density profile, we adopted an idealized model

of a cylindrical filament with radial density and column density profiles (as a function of cylindrical radius r) of the form:

$$\rho_p(r) = \frac{\rho_c}{[1 + (r/R_{\text{flat}})^2]^{p/2}} \rightarrow \Sigma_p(r) = A_p \frac{\rho_c R_{\text{flat}}}{[1 + (r/R_{\text{flat}})^2]^{p/2}}, \quad (1)$$

where $\Sigma = \mu m_{\text{H}} N_{\text{H}_2}$, $\mu = 2.33$ is the mean molecular mass, $A_p = \frac{1}{\cos i} \int_{-\infty}^{\infty} \frac{du}{(1+u^2)^{p/2}}$ is a finite constant factor for $p > 1$, ρ_c is the density at the center of the filament, and R_{flat} is the characteristic radius of the flat inner portion of the density profile¹. For simplicity, the inclination angle i of the model filament to the plane of the sky is assumed here to be $i = 0$ (but see online Appendix A for the effect of $i \neq 0$). At large radii ($r \gg R_{\text{flat}}$), the model density profile approaches a power law: $\rho_p(r) \sim \rho_c (r/R_{\text{flat}})^{-p}$. An important special case is the Ostriker (1964) model of an isothermal filament in hydrostatic equilibrium, for which $p = 4$, $A_p = \pi/2$, and R_{flat} corresponds to the thermal Jeans length at the center of the filament, i.e., $R_{\text{flat}} \equiv \lambda_J(r=0) = c_s^2 / (G\Sigma_{r=0})$.

When fitting such a model profile to the observations, ρ_c , R_{flat} , and p , along with the peak position of the filament, were treated as free parameters. The results (see, e.g., Fig. 2 and online Table 1) show that the observed profiles are generally well fitted with $1.5 < p < 2.5$. None of the observed filaments has the steep $p = 4$ density profile of the Ostriker (1964) model. A similar conclusion was already reported by Lada et al. (1999) in the case of the main streamer (i.e., Filament 6 here).

The above radial profile analysis can also be used to derive accurate masses per unit length, M_{line} , for the filaments by integrating column density over radius: $M_{\text{line}} = \int \Sigma_{\text{obs}}(r) dr$. The main source of uncertainty lies in the difficulty of defining the edges of the filaments, especially in crowded regions. The method is nevertheless quite robust when the bounds of integration are reasonably well defined (cf. Fig. 2). The values of

¹ Model profiles of the form described by Eq. (1) are sometimes called Plummer-like (cf. Nutter et al. 2008, and references therein). When R_{flat} is much smaller than the spatial resolution of the observations, such profiles are effectively equivalent to power laws.

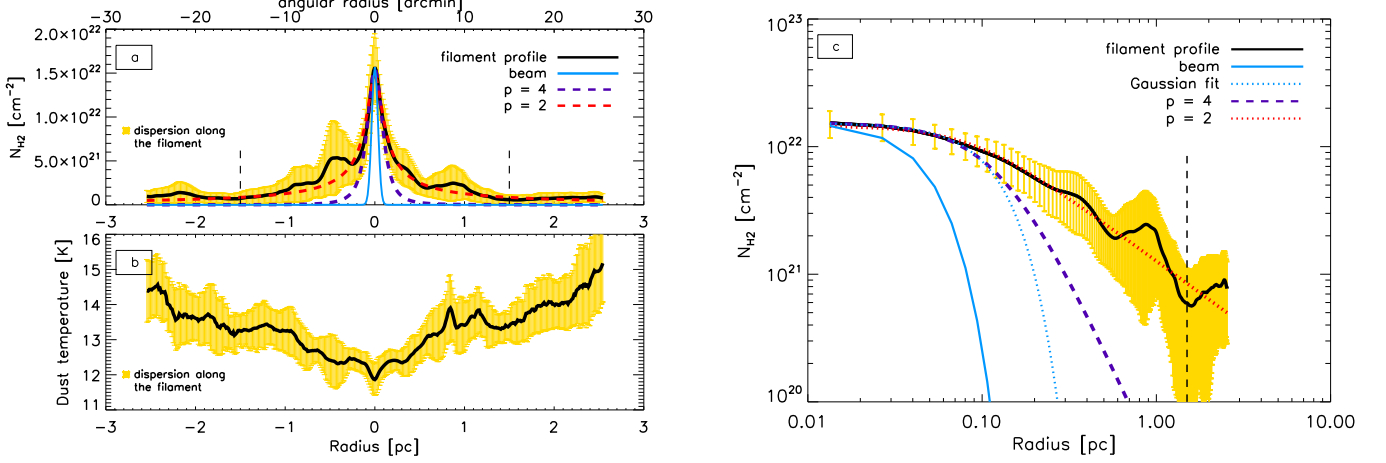


Fig. 2. (a) Mean radial column density profile perpendicular to the supercritical filament labeled 6 in Fig. 1b (black curve). The area in yellow shows the dispersion of the radial profile along the filament. The inner curve in light blue corresponds to the effective 36.9'' HPBW resolution (0.08 pc at 460 pc) of the column density map of Fig. 1a used to construct the profile. The dotted red curve shows the best-fit model of the form expressed by Eq. (1), with $p = 2$. For comparison, the dashed blue curve shows a model with $p = 4$, corresponding to a hydrostatic isothermal equilibrium filament (Ostriker 1964). The two dashed vertical segments at $\sim \pm 1.5$ pc mark the bounds within which the profile was integrated to estimate the mass per unit length M_{line} . (b) Mean radial dust temperature profile measured perpendicular to filament 6. (c) Same as (a) displayed in log-log format to better visualize the flatter inner part of the profile and the power-law behavior at large radii.

M_{line} derived with this method (see online Table 1) are typically 20% higher than simpler estimates assuming that the filaments have Gaussian column density profiles (cf. Appendix of André et al. 2010). Most bound prestellar cores appear to be located within supercritical, gravitationally unstable filaments with $M_{\text{line}} > M_{\text{line,crit}}$ (e.g. Filament 6 – see online Fig. 6b), a similar result to that already obtained by André et al. (2010) in Aquila. Note that both methods of estimating M_{line} (profile integration or Gaussian approximation) yield essentially the same conclusion on the gravitational instability of the filaments.

4. A characteristic width for interstellar filaments ?

To construct a reliable distribution of filament widths (cf. online Fig. 7a), we applied Gaussian fits to the radial column density profiles, as these tend to be more robust than the more sophisticated fits discussed in Sect. 3.2. A Gaussian fit to a model profile of the form of Eq. (1) with $p = 2$ indicates that the derived FWHM width is equivalent to $\sim 1.5 \times (2R_{\text{flat}})$. It can be seen in Fig. 7a that the filaments of IC5146 have a narrow distribution of deconvolved FWHM widths centered around a typical (median) value of 0.10 ± 0.03 pc (see also Fig. 3). Note that the same filaments span more than an order of magnitude in central column density (cf. online Table 1), implying a distribution of central Jeans lengths $[\lambda_J(r=0) = c_s^2 / (G\Sigma_{r=0})]$ from ~ 0.02 pc to > 0.3 pc, which is much broader than the observed distribution of widths (see Fig. 3 and blue dashed line in Fig. 7a).

In order to check that the measured filament widths were not strongly affected by the finite resolution of the column density map, we performed the same radial profile analysis using the SPIRE 250 μm map, which has a factor ~ 2 better resolution (18.1'' HPBW). The resulting distribution of filament widths is shown as a dotted histogram in online Fig. 7a and is statistically very similar to the original distribution at 36.9'' resolution (at the 50% confidence level according to a Kolmogorov-Smirnov test).

We also performed a similar analysis of the filamentary structure in two other regions located at different distances, the

Aquila and Polaris fields, also observed by us with *Herschel*. The Aquila region is a very active star-forming complex at $d \sim 260$ pc (e.g. Bontemps et al. 2010, and references therein), while the Polaris field is a high-latitude *translucent* cloud with little to no star formation at $d \sim 150$ pc (e.g. Ward-Thompson et al. 2010, and references therein). Following the same procedure as in Sect. 3.1, we identified 32 filaments in Aquila and 31 filaments in Polaris spanning three orders of magnitude in central column density from $\sim 10^{20} \text{ cm}^{-2}$ for the most tenuous filaments of Polaris to $\sim 10^{23} \text{ cm}^{-2}$ for the densest filaments of Aquila (see also Fig. 1 of André et al. 2010). The distribution of deconvolved FWHM widths for the combined sample of 90 filaments is shown in online Fig. 7b. This combined distribution is sharply peaked at 0.10 ± 0.03 pc, which strengthens the trend noted above for IC5146. While further tests would be required to fully investigate potential biases (especially given uncertainties in cloud distances – see Appendix A) and reach a definitive conclusion, our present findings suggest that most interstellar filaments may share a similar characteristic width of ~ 0.1 pc.

5. Discussion

The results presented in Sect. 3 and Sect. 4 can be used to discuss the formation and evolution of the observed filamentary structure. Three broad classes of models have been proposed in the literature to account for filaments in molecular clouds, depending on whether global gravity (e.g. Heitsch et al. 2008), magnetic fields (e.g. Nakamura & Li 2008), or large-scale turbulence (e.g. Padoan et al. 2001; Mac Low & Klessen 2004) play the dominant role. Large-scale gravity can hardly be invoked to form filaments in gravitationally unbound complexes such as the Polaris flare cloud (cf. Heithausen & Thaddeus 1990). While magnetic fields may play an important role in channeling mass accumulation onto the densest filaments (e.g. Goldsmith et al. 2008, Nakamura & Li 2008), our *Herschel* findings appear to be consistent with the turbulent picture. In the scenario proposed by Padoan et al. (2001), the filaments correspond to dense, post-

shock stagnation gas associated with regions of converging supersonic flows. One merit of this scenario is that it provides an explanation for the typical ~ 0.1 pc width of the filaments as measured with *Herschel* (Sect. 4 and Fig. 3). In a plane-parallel shock, the thickness λ of the postshock gas layer/filament is related to the thickness L of the preshock gas by $\lambda \approx L/M(L)^2$, where $M(L)$ is the Mach number and $M(L)^2$ is the compression ratio of the shock for a roughly isothermal radiative hydrodynamic shock. Thus, the thickness λ is independent of the scale L given Larson's linewidth-size relation [$M(L) \propto \sigma_v(L) \propto L^{0.5}$]. In this picture, the postshock thickness of the filaments effectively corresponds to the sonic scale λ_s at which the 3D turbulent velocity dispersion equals the sound speed (i.e., $M(\lambda_s) = 1$), leading to $\lambda \approx \lambda_s \sim 0.05\text{--}0.15$ pc according to recent determinations of the linewidth-size relationship in molecular clouds (e.g. Heyer et al. 2009; Federrath et al. 2010).

If large-scale turbulence provides a plausible mechanism for *forming* the filaments, the fact that prestellar cores tend to form in gravitationally unstable filaments (André et al. 2010) suggests that gravity is a major driver in the subsequent *evolution* of the filaments. The power-law shape of the outer density profiles, especially in the case of supercritical filaments (Sect. 3.2 and Fig. 2), is also suggestive of the role of gravity. Although the observed profiles are shallower than the profile of a self-gravitating isothermal equilibrium filament (Ostriker 1964), they are consistent with some models of magnetized filaments in gravitational virial equilibrium (Fiege & Pudritz 2000). Another attractive explanation of the observed $\rho \sim r^{-2}$ profiles is that the filaments are not strictly isothermal and that some of them are collapsing. Nakamura & Umemura (1999) have shown that the cylindrical version of the Larson-Penston similarity solution for the collapse of a filament has an outer density profile which approaches $\rho \propto r^{-2}$ when the equation of state is not isothermal but polytropic ($P \propto \rho^\gamma$) with $\gamma \lesssim 1$. The dust temperature profiles derived for the IC5146 filaments generally show a slight, but significant temperature drop toward the center of the filaments (cf. Fig. 2b), suggesting that a polytropic equation of state with $\gamma \lesssim 1$ may indeed be more appropriate than a simple isothermal assumption.

The lack of anti-correlation between filament width and central column density (see Fig. 3) provides another strong constraint on filament evolution. If the filaments are initially formed with a characteristic thickness ~ 0.1 pc as a result of turbulent compression (see above), then the left-hand (subcritical) side of Fig. 3 can be readily understood. The right-hand (supercritical) side of Fig. 3 is more surprising since one would naively expect an anti-correlation between width and central column density (e.g. $W \propto 1/\Sigma_0$) for self-gravitating filaments contracting at fixed mass per unit length. However, the velocity dispersion σ_v and the virial mass per unit length, $M_{\text{line,vir}} = 2\sigma_v^2/G$ (replacing $M_{\text{line,crit}}$ in the presence of nonthermal motions – see Fiege & Pudritz 2000), may increase during filament contraction as gravitational energy is converted into kinetic energy. If approximate virial balance is maintained, the width $\sim \sigma_v^2/(G\Sigma_0)$ may thus remain nearly constant as in Fig. 3. A trend such as $\sigma_v \propto \Sigma^{0.5}$ has indeed been found by Heyer et al. (2009) in their study of velocity dispersions in Galactic molecular clouds. To account for the right-hand side of Fig. 3, we thus hypothesize that gravitationally unstable filaments may accrete additional mass from their surroundings and *increase in mass per unit length* while contracting. Interestingly, mass accretion onto the densest filaments of Taurus and Cygnus X may have been observed in the form of CO striations aligned with the local magnetic field (Goldsmith et al. 2008; Nakamura & Li 2008; Schneider et al. 2010). Molecular line observations (cf. Kramer et al. 1999) of a broad sample of

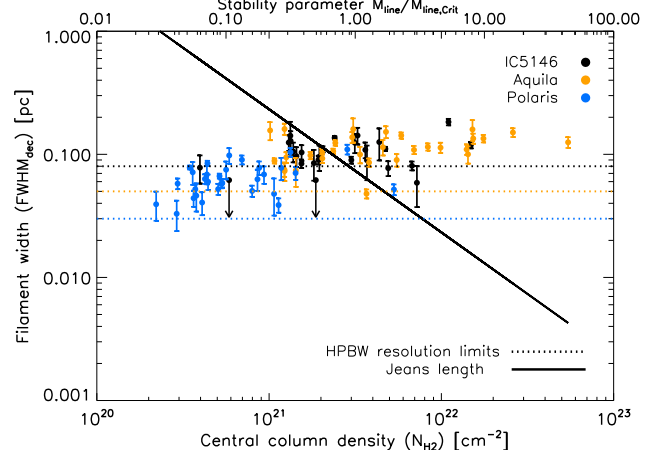


Fig. 3. Mean deconvolved width (FWHM) versus mean central column density for the 27 filaments of IC5146 shown in Fig. 1b, along with 32 filaments in Aquila and 31 filaments in Polaris, all analyzed in the same way (see Sect. 3). The spatial resolutions of the column density maps used in the analysis for the three regions are marked by the horizontal dotted lines. The filament width has a typical value of ~ 0.1 pc, regardless of central column density. The solid line running from top left to bottom right shows the central (thermal) Jeans length as a function of central column density [$\lambda_J = c_s^2/(G\Sigma_0)$] for a gas temperature of 10 K.

Herschel filaments in several regions would be extremely valuable to confirm the validity of the scenario proposed here.

Acknowledgements. SPIRE has been developed by a consortium of institutes led by Cardiff Univ. (UK) and including Univ. Lethbridge (Canada); NAOC (China); CEA, LAM (France); IFSI, Univ. Padua (Italy); IAC (Spain); Stockholm Observatory (Sweden); Imperial College London, RAL, UCL-MSSL, UKATC, Univ. Sussex (UK); Caltech, JPL, NHSC, Univ. Colorado (USA). This development has been supported by national funding agencies: CSA (Canada); NAOC (China); CEA, CNES, CNRS (France); ASI (Italy); MCINN (Spain); SNSB (Sweden); STFC (UK); and NASA (USA). PACS has been developed by a consortium of institutes led by MPE (Germany) and including UVIE (Austria); KUL, CSL, IMEC (Belgium); CEA, OAMP (France); MPIA (Germany); IFSI, OAP/AOT, OAA/CAISMI, LENS, SISSA (Italy); IAC (Spain). This development has been supported by the funding agencies BMVIT (Austria), ESA-PRODEX (Belgium), CEA/CNES (France), DLR (Germany), ASI (Italy), and CICT/MCT (Spain).

References

- André, P., Men'shchikov, A., Bontemps, S., et al. 2010, *A&A*, 518, L102+
- Balsara, D., Ward-Thompson, D., & Crutcher, R. M. 2001, *MNRAS*, 327, 715
- Bontemps, S., André, P., Könyves, V., et al. 2010, *A&A*, 518, L85+
- Federrath, C., Roman-Duval, J., Klessen, R. S., Schmidt, W., & Mac Low, M. 2010, *A&A*, 512, A81+
- Fiege, J. D. & Pudritz, R. E. 2000, *MNRAS*, 311, 85
- Goldsmith, P. F., Heyer, M., Narayanan, G., et al. 2008, *ApJ*, 680, 428
- Griffin, M. J., Abergel, A., Abreu, A., et al. 2010, *A&A*, 518, L3+
- Harvey, P. M., Huard, T. L., Jørgensen, J. K., et al. 2008, *ApJ*, 680, 495
- Heithausen, A. & Thaddeus, P. 1990, *ApJ*, 353, L49
- Heitsch, F., Hartmann, L. W., Slyz, A. D., Devriendt, J. E. G., & Burkert, A. 2008, *ApJ*, 674, 316
- Heyer, M., Krawczyk, C., Duval, J., & Jackson, J. M. 2009, *ApJ*, 699, 1092
- Hildebrand, R. H. 1983, *QJRAS*, 24, 267
- Inutsuka, S. & Miyama, S. M. 1997, *ApJ*, 480, 681
- Könyves, V., André, P., Men'shchikov, A., et al. 2010, *A&A*, 518, L106+
- Kramer, C., Alves, J., Lada, C. J., et al. 1999, *A&A*, 342, 257
- Kramer, C., Richer, J., Mookerjee, B., Alves, J., & Lada, C. 2003, *A&A*, 399, 1073
- Lada, C. J., Alves, J., & Lada, E. A. 1999, *ApJ*, 512, 250
- Lada, C. J., Lada, E. A., Clemens, D. P., & Bally, J. 1994, *ApJ*, 429, 694

- Mac Low, M. & Klessen, R. S. 2004, *Reviews of Modern Physics*, 76, 125
- McKee, C. F. & Ostriker, E. C. 2007, *ARA&A*, 45, 565
- Men'shchikov, A., André, P., Didelon, P., et al. 2010, *A&A*, 518, L103+
- Miville-Deschênes, M., Martin, P. G., Abergel, A., et al. 2010, *A&A*, 518, L104+
- Molinari, S., Swinyard, B., Bally, J., et al. 2010, *A&A*, 518, L100+
- Nakamura, F. & Li, Z. 2008, *ApJ*, 687, 354
- Nakamura, F. & Umemura, M. 1999, *ApJ*, 515, 239
- Nutter, D., Kirk, J. M., Stamatellos, D., & Ward-Thompson, D. 2008, *MNRAS*, 384, 755
- Ostriker, J. 1964, *ApJ*, 140, 1056
- Padoan, P., Juvela, M., Goodman, A. A., & Nordlund, Å. 2001, *ApJ*, 553, 227
- Pilbratt, G. L., Riedinger, J. R., Passvogel, T., et al. 2010, *A&A*, 518, L1+
- Poglitsch, A., Waelkens, C., Geis, N., et al. 2010, *A&A*, 518, L2+
- Schneider, N., Csengeri, T., Bontemps, S., et al. 2010, *A&A*, 520, A49+
- Sousbie, T. 2011, *MNRAS* in press (cf. ArXiv:1009.4015)
- Stark, J. L., Donoho, D. L., & Candès, E. J. 2003, *A&A*, 398, 785
- Ward-Thompson, D., Kirk, J. M., André, P., et al. 2010, *A&A*, 518, L92+

¹ Laboratoire AIM, CEA/DSM-CNRS-Université Paris Diderot, IRFU/Service d'Astrophysique, C.E.A. Saclay, Orme des Merisiers, 91191 Gif-sur-Yvette, France e-mail: doris.arzoumanian@cea.fr, pandre@cea.fr

² Institut d'Astrophysique de Paris, UMR 7095 CNRS, Université Pierre et Marie Curie, 98 bis Boulevard Arago, F-75014 Paris, France

³ Laboratoire d'Astrophysique de Marseille, CNRS/INSU-Université de Provence, 13388 Marseille cedex 13, France

⁴ Université de Bordeaux, OASU, Bordeaux, France

⁵ National Research Council of Canada, Herzberg Institute of Astrophysics, University of Victoria, Department of Physics and Astronomy, Victoria, Canada

⁶ School of Physics & Astronomy, Cardiff University, Cardiff, UK

⁷ Canadian Institute for Theoretical Astrophysics, University of Toronto, Toronto, ON M5S 3H8, Canada

⁸ IFSI - INAF, via Fosso del Cavaliere 100, I-00133 Roma, Italy

⁹ The Rutherford Appleton Laboratory, Chilton, Didcot OX11 0NL, UK

¹⁰ Department of Physics and Astronomy, McMaster University, Hamilton, ON L8S 4M1, Canada

¹¹ Department of Physics & Astronomy, The Open University, Milton Keynes, UK

Appendix A: Effects of distance and dust opacity uncertainties and influence of the viewing angle

There is some ambiguity concerning the distance to IC5146. The default distance adopted in this paper corresponds to the value of 460^{+40}_{-60} pc derived from star counts by Lada et al. (1999). However, other studies placed the IC5146 cloud at a distance of 950 ± 80 pc based on photometry and spectra of late-B stars in the IC5146 cluster (e.g. Harvey et al. 2008). If the true distance of IC5146 were ~ 950 pc instead of ~ 460 pc, then the widths of the IC5146 filaments would all be a factor of ~ 2 larger than the values listed in Col. 6 of Table 1, leading to a median width of $z = 0.2 \pm 0.06$ pc instead of 0.1 ± 0.03 pc. This would also broaden the distribution of FWHM widths for the combined sample of 90 filaments in IC5146, Aquila, and Polaris (see dotted histogram in online Fig. 7b). As can be seen in online Fig. 7b, our main result that the typical filament width is ~ 0.1 pc to within a factor of ~ 2 would nevertheless remain valid. We also stress that the distance uncertainty has no effect on the *shape* of the radial column density profiles (Sect. 3.2 and Fig. 2) or on the absence of an anti-correlation between filament width and central column density in Fig. 3.

The following (temperature-independent) dust opacity law was assumed in our analysis of the *Herschel* data: $\kappa_\nu = 0.1 \times (\nu/1000 \text{ GHz})^2 \text{ cm}^2/\text{g}$, where ν denotes frequency and κ_ν is the dust opacity per unit (gas + dust) mass column density. This dust opacity law is very similar to that advocated by Hildebrand (1983) at submillimeter wavelengths, and is consistent with the mean value $\kappa_{850\mu} \approx 0.01 \text{ cm}^2/\text{g}$ derived by Kramer et al. (2003) in IC5146 from a detailed comparison of their SCUBA 850 μm and 450 μm data with the near-infrared extinction map of Lada et al. (1999). However, Kramer et al. (2003) found evidence of an increase in the dust opacity $\kappa_{850\mu}$ by a factor of ~ 4 when the dust temperature T_d decreased from ~ 20 K to ~ 12 K, which they interpreted as the manifestation of dust grain evolution (e.g. coagulation and formation of ice mantles) in the cold, dense interior of the cloud. The dust temperature map derived from *Herschel* data (see Fig. 6a) suggests that T_d ranges from ~ 11 K to ~ 17 K in the bulk of IC5146, with the exception of the PDR region associated with the Cocoon Nebula where T_d reaches ~ 30 K. Assuming a linear increase in κ_ν by a factor of 4 when T_d decreases from ~ 20 K to ~ 12 K as suggested by the Kramer et al. (2003) study, we estimate that the column density map shown in Fig. 1a is accurate to better than a factor of ~ 2 over most of its extent. The possible dependence of κ_ν on temperature has very little impact on our analysis of the filament profiles. For filament 6, for instance, T_d decreases by less than ~ 3 K from the exterior to the interior of the filament (see Fig. 2b), suggesting that κ_ν does not change by more than $\sim 40\%$ from large to small radii. The potential effect on the estimated FWHM width, W , and power-law index, p , of the filament profiles is even smaller: W would increase, and p would decrease, by less than $\sim 3\%$ and $\sim 7\%$, respectively.

Our *Herschel* observations only provide information on the *projected* column density profile $\Sigma_{\text{obs}}(r) = \frac{1}{\cos i} \Sigma_{\text{int}}(r)$ of any given filament, where i is the inclination angle to the plane of the sky and Σ_{int} is the intrinsic column density profile of the filament. For a population of randomly oriented filaments with respect to the plane of the sky, the net effect is that Σ_{obs} *overestimates* Σ_{int} by a factor $\langle \frac{1}{\cos i} \rangle = \frac{\pi}{2} \sim 1.57$ on average. This does not affect our analysis of the shape of the radial column density profiles (Sect. 3.2), but implies that the central column densities of the filaments are actually $\sim 60\%$ lower on average than the projected values listed in Col. 2 of Table 1. Likewise,

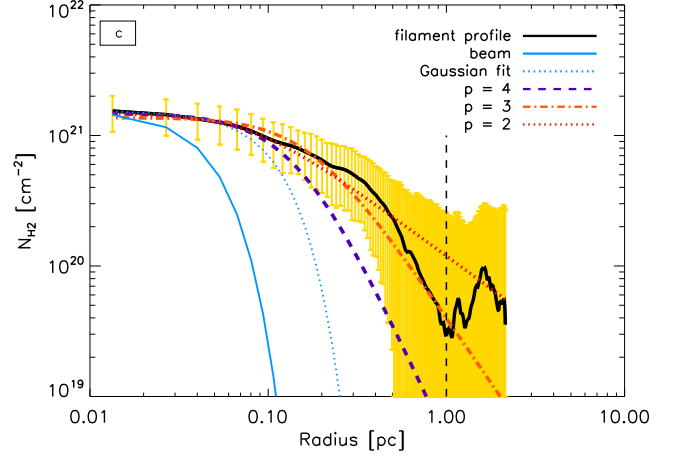


Fig. 4. Mean radial column density profile in log-log format of the subcritical filament labeled 14 in Fig. 1b (western side). Note that, given the relatively large dispersion of the radial profile along the filament (shown in yellow), the power-law behavior at large radii is less clear in this subcritical case than for the supercritical filament shown in Fig. 2c.

the observed masses per unit length (Col. 12 of Table 1) tend to overestimate the true masses per unit length of the filaments by $\sim 60\%$ on average. Although systematic, this inclination effect remains less than a factor of 2 and thus has little impact on the classification of observed filaments in thermally subcritical and thermally supercritical filaments.

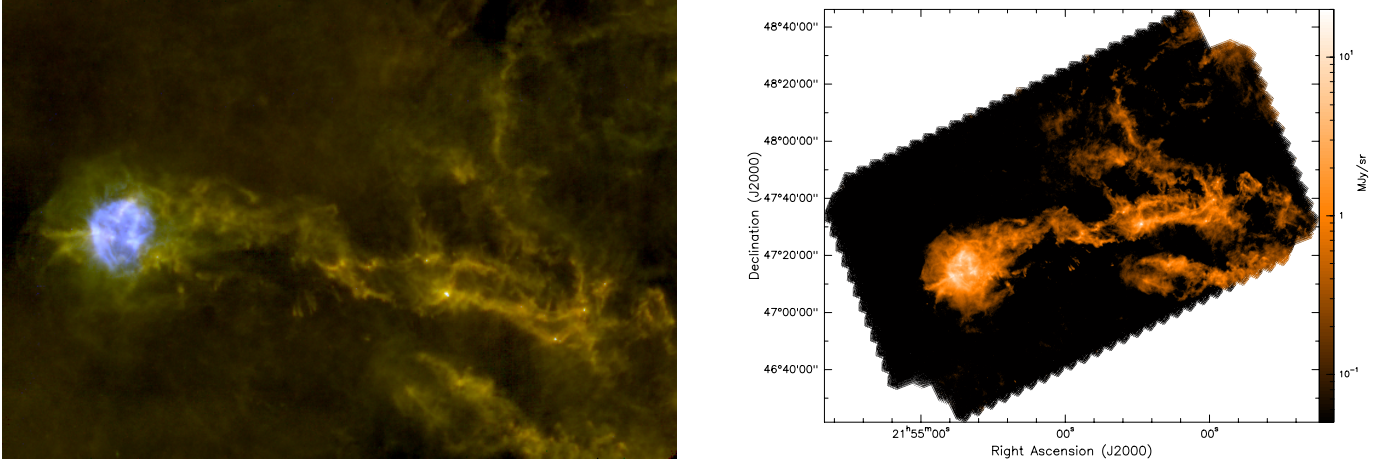


Fig. 5. (a) Composite 3-color image of IC5146 ($\sim 1.6 \text{ deg}^2$ field) produced from our PACS/SPIRE parallel-mode data at 70, 250, and $500 \mu\text{m}$. The color coding is such that red = SPIRE $500 \mu\text{m}$, green = SPIRE $250 \mu\text{m}$, blue = PACS $70 \mu\text{m}$. (b) SPIRE $250 \mu\text{m}$ image of IC5146.

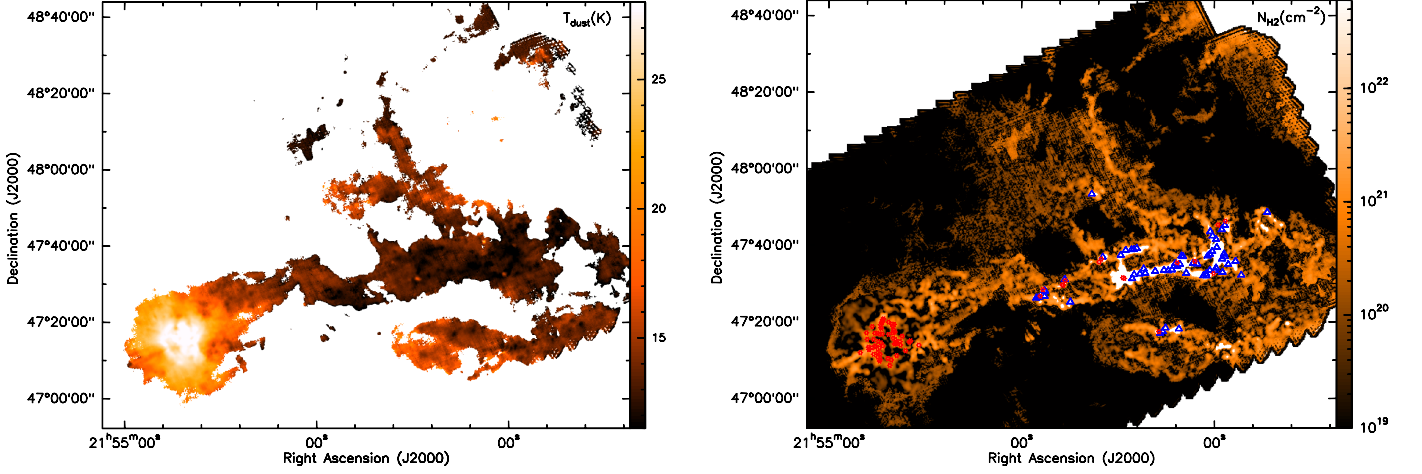


Fig. 6. (a) Dust temperature map derived from our SPIRE/PACS observations of IC5146. The resolution corresponds to the $36.9''$ HPBW resolution of SPIRE at $500 \mu\text{m}$. (b) Curvelet component of the column density map of IC5146 (cf. Fig. 1), in which the areas where the filaments have a mass per unit length larger than half the critical value and are thus likely gravitationally unstable have been highlighted in white. The positions of the 71 YSOs and 45 candidate bound prestellar cores identified with *getsources* (Men'shchikov et al. 2010) in the *Herschel* images are overplotted as red stars and dark blue triangles, respectively. Candidate bound prestellar cores were selected among a larger population of starless cores (see blue triangles in Fig. 1a), on the basis of a comparison of the core masses with local values of the Jeans or Bonnor-Ebert mass (see Sect. 4.1 of Könyves et al. 2010, for details). Note the excellent correspondence between the spatial distribution of the prestellar cores and the supercritical filaments, in agreement with our earlier results in Aquila and Polaris (see Fig. 2 of André et al. 2010).

Table 1. Summary of derived parameters for the 27 filaments of IC5146

Filament	$N_{\text{H}_2}^0$ [10^{21} cm^{-2}]	$\sigma_{N_{\text{H}_2}}^{(a)}$	T_d^0	$\sigma_{T_d}^{(a)}$	$\langle \text{FWHM}_{\text{dec}} \rangle$	$\sigma_{\langle \text{FWHM}_{\text{dec}} \rangle}^{(a)}$	λ_J^0	$\sigma_{\lambda_J}^{(a)}$	$p^{(b)}$	$R_{\text{flat}}^{(b)}$	$M_{\text{line}}^{(c)}$
(1)	(2)	(3)	(4)	(5)	(6)	(7)	(8)	(9)	(10)	(11)	(12)
1	1.8	0.2	15.4	0.6	0.12	0.02	0.11	0.09	2.1	0.05	9
2	4.8	4.4	13.9	0.7	0.11	0.03	0.07	0.09	1.9	0.06	21
3	1.6	0.3	12.6	0.5	0.11	0.02	0.07	0.05	–	–	2
4	1.6	0.5	13.5	0.5	0.10	0.06	0.09	0.07	1.4	0.02	8
5	7.5	4.5	12.1	0.6	0.06	0.05	0.04	0.04	1.5	0.01	28
6	16	7.6	11.8	0.9	0.12	0.04	0.02	0.01	1.7	0.04	152
7	5.6	2.4	12.1	0.5	0.09	0.04	0.03	0.02	1.6	0.03	22
8	2.0	0.7	13.6	0.5	0.08	0.03	0.15	0.01	1.5	0.05	6
9	3.3	1.3	12.5	0.3	0.14	0.02	0.05	0.06	1.5	0.04	10
10	3.3	0.6	13.6	0.4	0.14	0.03	0.10	0.02	2.1	0.06	14
11	5.3	2.5	11.7	0.5	0.08	0.03	0.05	0.03	1.9	0.04	15
12	12	4.1	11.7	1.0	0.18	0.03	0.02	0.01	1.5	0.03	41
13	6.9	5.8	12.7	0.8	0.08	0.03	0.04	0.09	1.6	0.02	23
14 ^(d)	1.5	0.8	13.7	0.5	0.13	0.03	0.21	0.01	1.5–2.4	0.04–0.14	13
15	2.1	2.2	14.7	1.1	0.11	0.04	0.16	0.06	–	–	4
16 ^(e)	3.3	0.9	26.9	2.1	0.12	0.02	0.19	0.05	–	–	12
17 ^(e)	2.0	1.7	18.3	2.9	0.09	0.05	0.20	0.29	1.3	0.04	6
18 ^(e)	3.9	2.0	22.2	2.6	0.11	0.04	0.12	0.09	–	–	49
19 ^(e)	3.6	1.5	26.5	1.2	0.09	0.03	0.17	0.08	1.9	0.08	1
20	0.57	0.5	15.5	0.5	0.08	0.02	0.24	0.01	1.5	0.03	3
21	1.5	0.5	14.0	0.4	0.13	0.03	0.09	0.06	1.7	0.05	6
22 ^(f)	0.8	0.1	13.5	0.3	< 0.06	0.19	0.32	0.05	–	–	1
23 ^(d)	1.4	0.4	13.2	0.7	0.14	0.07	0.09	0.07	1.5–1.8	0.04–0.06	7
24	5.6	1.1	12.3	0.2	0.07	0.03	0.05	0.01	–	–	21
25	2.2	1.5	12.7	0.5	0.10	0.03	0.09	0.01	1.5	0.03	11
26 ^(d)	1.5	0.3	12.5	0.4	0.10	0.06	0.19	0.04	1.5–2.1	0.05–0.08	2
27 ^(f)	2.9	1.0	11.5	0.3	< 0.06	0.03	0.03	0.03	1.4	0.02	13
mean	3	1	13.5	0.5	0.10	0.03	0.09	0.05	1.6	0.03	11
range	0.6–16	0.1–7.6	11–27	0.2–2.9	0.06–0.18	0.02–0.19	0.02–0.32	0.01–0.29	1.3–2.4	0.01–0.08	1–152
rms	3.4	1.9	4.1	0.7	0.03	0.03	0.07	0.06	0.3	0.02	30

Notes: Col. 2, Col. 4, Col. 8: Mean projected column density, dust temperature, and Jeans length estimated at the center of each filament. Col. 6: Weighted mean of the distribution of deconvolved FWHM widths resulting from Gaussian fits to the radial profiles at each position along the filament. ^(a) The quoted dispersion is the standard deviation of the *distribution* of the measured parameter along each filament. In the case of $\langle \text{FWHM}_{\text{dec}} \rangle$ (Col. 6), this dispersion (Col. 7) is larger than the error bar plotted in Fig. 3 which corresponds to the standard deviation of the *mean* deconvolved FWHM width. ^(b) p and R_{flat} correspond to the best-fit model of the form expressed by Eq. (1) to the mean column density profile of each filament. The fit was weighted by $1/\sigma(r)^2$ where $\sigma(r)$ is the standard deviation of the radial profile at projected radius r , estimated from the measured (1σ) dispersion along the filament. The same bounds (shown as vertical dashed lines in Figs. 2a, 2c, 4 for filaments 6 and 14) were used to fit the profiles and to calculate the mass per unit length by integrating over the radial profile. ^(c) Col. 12 gives to the projected mass per unit length obtained by integrating over the observed column density profile of each filament. The thermally supercritical filaments with $M_{\text{line}} > M_{\text{line,crit}}$ are indicated in boldface, where $M_{\text{line,crit}} = 2c_s^2/G \sim 20 M_{\odot}/\text{pc}$ (for a gas temperature $T \sim 12$ K, corresponding to the median central dust temperature measured here, ignoring the temperatures of the filaments located in the PDR region). ^(d) Filaments 14, 23, and 26 have asymmetric radial profiles. A separate fit was thus performed on either side of each of these three filaments. The values of p and R_{flat} reported in Col. 10 and Col. 11 correspond to the best-fit values on either side of these filaments. ^(e) Filaments 16, 17, 18, and 19 are located in the PDR region called the *Cocoon Nebula* (see Fig. 1a and online Fig. 5), and their derived dust temperatures may be overestimated. ^(f) Filaments 22 and 27 have unresolved widths and are shown as upper limits corresponding to 75% of the HPBW resolution in Fig. 3.

Table 2. Median values of observed angular widths and deconvolved physical widths^(a) for three samples of filaments and two angular resolutions

Field	distance [pc]	From column density maps with 36.9'' resolution				From SPIRE 250 μ m images with 18.1'' resolution			
		FWHM _{obs} ['']	$\sigma_{\text{FWHM}_{\text{obs}}}$ ['']	FWHM _{dec} [pc]	$\sigma_{\text{FWHM}_{\text{dec}}}$ [pc]	FWHM _{obs} ['']	$\sigma_{\text{FWHM}_{\text{obs}}}$ ['']	FWHM _{dec} [pc]	$\sigma_{\text{FWHM}_{\text{dec}}}$ [pc]
(1)	(2)	(3)	(4)	(5)	(6)	(7)	(8)	(9)	(10)
IC5146	460	59	15	0.10	0.03	44	10	0.09	0.02
Aquila	260	94	21	0.11	0.03	97	31	0.12	0.04
Polaris	150	94	24	0.06	0.02	74	20	0.05	0.02
All ^(b)				0.10	0.03			0.09	0.02

Notes: Col. 3 and Col. 7: Median value of the observed FWHM angular width before deconvolution. Col. 5 and Col. 9: Median value of the deconvolved FWHM physical width. Col. 4, Col. 6, Col. 8, Col. 10: Dispersion (standard deviation) of the distribution of widths for each filament sample. ^(a) The DisPerSE algorithm (Sousbie 2011) we used to trace filaments in the column density maps derived from *Herschel* data does not consider filamentary width in its process of identifying filaments. While it is difficult to assess the completeness of our census of filamentary structures without dedicated tests (which will be the subject of future work), there is in principle no bias toward selecting structures of similar width with DisPerSE. ^(b) The last row refers to the combined sample of 90 filaments observed in IC5146, Aquila, and Polaris.

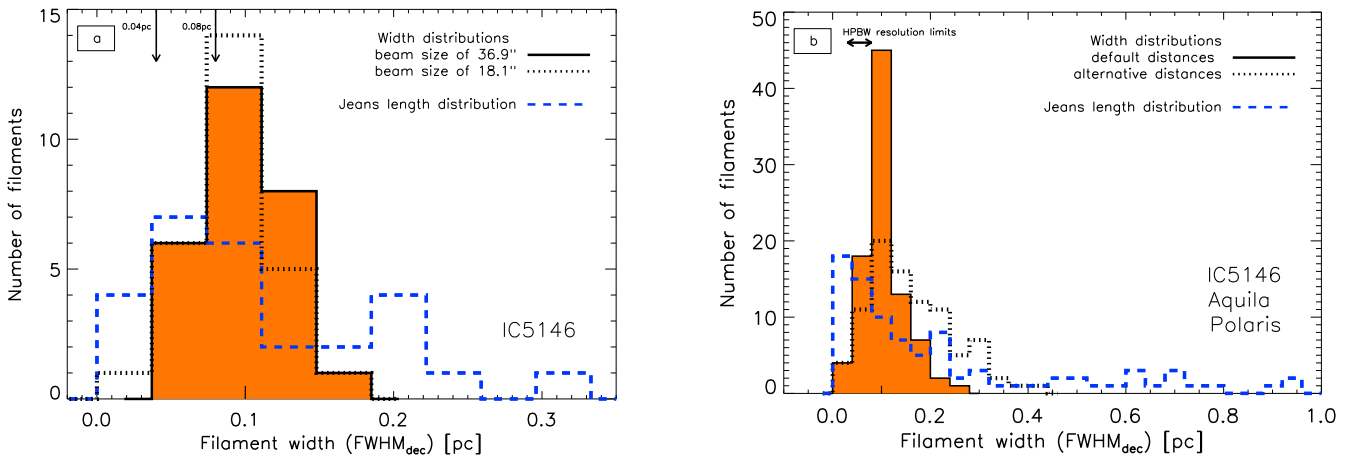


Fig. 7. (a) Distribution of deconvolved FWHM widths for the 27 filaments of IC5146 (black solid histogram, filled in orange). These widths have been deconvolved from the 36.9'' HPBW resolution of the column density map (Fig. 1a) used to construct the radial profiles of the filaments. The median width is 0.10 pc and the standard deviation of the distribution is 0.03 pc. The black dotted histogram shows the distribution of deconvolved FWHM widths measured on the SPIRE 250 μ m map which has a factor ~ 2 better resolution (18.1'' HPBW). This distribution is statistically indistinguishable from the distribution obtained at 36.9'' resolution. The two down pointing arrows in the upper left mark the resolution limits for the distributions at 36.9'' and 18.1'', i.e., 0.08 pc and 0.04 pc, respectively. For comparison, the blue dashed histogram represents the distribution of central Jeans lengths corresponding to the central column densities of the filaments. **(b)** Distributions of deconvolved FWHM widths for a larger sample of 90 filaments, combining the 27 filaments of IC5146, 32 filaments in Aquila, and 31 filaments in Polaris, all analyzed in the same way from column density maps with 36.9'' resolution as explained in Sect. 3 and Sect. 4. The black solid histogram, filled in orange, is based on our default distance assumptions: 460 pc for IC5146, 260 pc for Aquila, and 150 pc for Polaris. This distribution has a median of 0.10 pc and a standard deviation of 0.03 pc. The horizontal double arrow at the upper left shows the range of HPBW resolution limits, going from ~ 0.03 pc for Polaris to ~ 0.08 pc for IC5146. The dotted histogram shows an alternate distribution of deconvolved widths for the same sample of filaments based on other distance assumptions: 950 pc for IC5146 (see Appendix A), 400 pc for Aquila (see discussion in Bontemps et al. 2010, and Appendix of André et al. 2010), and 150 pc for Polaris. The median value of this alternate distribution is 0.15 pc and the standard deviation is 0.08 pc. For comparison, the blue dashed histogram represents the distribution of central Jeans lengths corresponding to the central column densities of the 90 filaments (independent of distance).